scientific reports

OPEN

Dynamic responses characteristics of bedrock and overburden layer slope with anchored frame piles based on shaking table test

Lei Wang[1], Qianhui Pu[1], Guangpeng Chen[1], Jing Lian[2✉], Changwei Yang[1] & Mingming Dai[1]

To adapt to higher and steeper slope environments, this paper proposes a new type of support structure called an anchored frame pile. The study designed and conducted a series of shaking table tests with three-way loading. The acceleration field of the slope, bedrock and overburden layer vibration variability, Fourier spectra, pile dynamic earth pressure, anchor cable force, and damage were analyzed in detail. The results indicate that the overall effectiveness of anchored frame piles for slope reinforcement is superior, and the synergistic impact of front and back piles is evident. Anchor cables effectively reduce the variability of bedrock and overburden layer vibrations. A zone of acceleration concentration always exists at the shoulder of a slope under seismic action. The dominant Fourier frequency in the Y direction of the slope is 11.7687 Hz under Wolong seismic, and the high-frequency vibrations of the upper overburden layer are significantly stronger than those of the bedrock. Slopes under 0.4 g earthquakes first form cracks at the top and then expand downward through them. Under seismic action, the peak dynamic earth pressure in front of the front pile occurs near the bottom of the pile, and the dynamic earth pressure behind the pile occurs near the slip surface. The peak dynamic earth pressure of the back pile occurs at the top of the bedrock. The slope damage is significant at 0.6 g. At this point, the peak dynamic soil pressure at the top of the front pile measures 9.5 kPa, while the peak dynamic soil pressure at the bottom reaches 24.3 kPa. Below the sliding surface of the front pile and on top of the bedrock of the back pile are the critical areas for prevention and control. Elevating the prestressing of the anchor cables will help enhance the synergy between the anchor cables and the piles. Simultaneously, it will reduce the variability of vibration in the bedrock and overburden, thereby improving the stability of the slopes.

China has complex topographic conditions. Two-thirds of the total area of the country is mountainous, so the construction of railroads and highways will certainly face a large number of slopes[1]. At present, the construction of high-speed railroads in mountainous areas faces challenges such as high altitudes, high intensity, heavy rainfall, and other harsh environments. These conditions directly impact the stability of slopes, leading to large-scale landslides that can compromise traffic safety. The most common anti-slip structure used in landslide management is the anchor cable anti-slip pile. However, when the scale of a landslide is large, it can result in significant displacement of the anti-slip piles, or even cause the anchoring section of the pile to reverse. Additionally, the pile body may become broken, among other issues. Therefore, proposing a new support structure will make it easier to withstand the influence of these complex and harsh environments, ensuring safe travel.

Currently, supporting structures such as anti-slip piles, anchor anti-slip piles, anchor frame beams, and gravity retaining walls have been widely used in landslide management. Earthquakes are one of the primary factors that cause landslides. Scholars both domestically and internationally have conducted extensive research on the dynamic response of slopes and traditional support structures through shaking table tests and numerical calculations[2–5]. Wu et al.[6] found that the damage pattern of fissured slopes was controlled by the fissures through

[1]MOE Key Laboratory of High-Speed Railway Engineering, School of Civil Engineering, Southwest Jiaotong University, Chengdu 610031, China. [2]School of Architecture and Civil Engineering, Xihua University, Chengdu 610039, China. ✉email: 781510224@qq.com

shaking table tests. The continuous expansion of the fissures led to the shear damage of slopes and the continuous formation of new fissures. Yang et al.[7] found that the increase in water content of a slope under frequent earthquakes will lead to a decrease in the natural frequency. They also observed that the natural frequency was more sensitive to earthquakes than the damping ratio. Through three-dimensional nonlinear finite element analysis. Lv et al.[8] found that the top of the slope may locally collapse under the influence of earthquakes or rainfall, and the anchor bolts can effectively enhance the local stability of the slope. It has been shown that the support structure can effectively improve slope stability. Currently, anchor cable anti-slip piles are extensively utilized in slope disaster control[9–12]. Xu et al.[13] conducted a variable parameter study of anti-slide piles using finite element analysis and recommended the optimal design for anti-slide piles. Hu et al.[14] investigated the seismic response and damage mechanism of anti-slide piles through a shaking table test. They found that the maximum bending moment of the anti-slide pile occurred near the middle of the slide. Dong et al.[15] developed a stability evaluation method for a multi-row anchor cable-anti-slide pile reinforced slope, taking into account the impact of prestress and pile body. They discovered that enhancing the prestress of the middle and lower anchor cables can significantly increase the safety factor of the slope. Based on the theory of the Winkler elastic foundation beam, Qu et al.[16] established the dynamic analytical solution for pile displacement, bending moment, and shear force of anchor pile-sheet wall. They verified this solution through experiments, providing a basis for the design of such structures. Chen et al.[17,18] found that the pile-anchor structure can effectively enhance the stability of the slope through a shaking table test. They observed that the peak value of soil pressure occurred near the sliding surface during an earthquake. Lian et al.[19] proposed a novel spatial anchor cable anti-slide pile structure that takes into account the strength of the surrounding rock and conducted a shaking table test. Under the action of an earthquake, acceleration concentration areas will appear on the surface layer, and these areas will move toward the anchorage section of the anchor cable as the earthquake intensifies.

It can be seen from the above results that shaking table tests and numerical simulations are commonly used methods for studying the dynamic response of slopes. Currently, the acceleration amplification effect on slopes is primarily analyzed at a single point along the elevation or slope change, without a comprehensive analysis of the entire slope acceleration field. This paper proposes a novel type of supporting structure known as an anchored frame pile, which is a super-statically determinate space structure characterized by significant overall stiffness. This design effectively mitigates deformation caused by landslides (rock piles). With strong integrity and excellent coordination, the local slope debris flow can safely traverse the top plate of the anchored frame structure. However, the current understanding of the dynamic response of this innovative structure under seismic action remains limited. Therefore, this paper presents a large-scale vibrating table test conducted on the proposed new anchored frame pile structure. The test aims to analyze the dynamic behavior of the slope, the forces acting on the supporting structure, and the safety of traffic. The findings will contribute to optimizing and advancing the application of this innovative structure.

Structural form

In this paper, a new slope support structure of anchored frame piles is proposed. The structure consists of front piles, back piles, cross beams, secondary beams, cover plates, anchor cables, and inter-pile supports. The front pile and the back pile are connected by cross beams and secondary beams. The front piles are equipped with multiple rows of anchor cables. The front piles are interconnected by inter-pile supports, and cover plates are installed between the crossbeams. Compared with traditional support structures such as anchor cable anti-slip piles, When the soil behind the pile slides and squeezes against the front pile, the thrust force on the front pile is transferred to the back pile through the crossbeam and secondary beam. The back piles and anchor cables can effectively enhance the bending resistance of the front piles. A train is traveling on top of the secondary beam. The cover plate at the top of the structure effectively prevents mudslides and falling rocks caused by landslides from affecting traffic safety. The specific structural form is shown in Fig. 1.

Shaking table test design
Testing facilities

The shaking table test was conducted at National Engineering Research Center of Geological Disaster Prevention Technology in Land Transportation. The shaking table parameters are shown in Table 1. The rigid model box used in this test consisted of steel plates, angle steel, and channel steel, with internal dimensions of 3.15 m × 2.30 m × 2.20 m (length × width × height). The model box was connected to the shaking table by high-strength bolts. A 12-megapixel industrial camera was mounted on top of the model to capture the entire test process. The shaking table and model box are shown in Fig. 2.

Scaling law and material

Shaking table test was a powerful tool for studying the dynamic response of slopes[20–23]. In this paper, based on the Buckingham π theorem[24], dimensional analysis was conducted to derive similarity parameters for other physical quantities using geometric dimension, density, and gravity acceleration as the control indices. As shown in Table 2. Due to the large number of model parameters involved in the test, it is challenging to ensure that all parameters exhibited the same level of similarity during the test. However, the test could still provide valuable guidance for engineering practice by revealing macroscopic damage patterns and consistent dynamic responses. In this paper, the similarity coefficients of 30, 1, and 1 were determined for the geometry dimension, density, and gravity acceleration, respectively, based on the model box dimensions. On this basis, the target soil parameters were determined through a direct shear test using gypsum, barite powder, quartz sand, glycerol, loess, and water as raw materials. The straight shear test is shown in Fig. 3. Bedrock and overburden layer parameters are shown in Table 3. The frame piles for this test were simulated using acrylic plates with cross-sectional dimensions
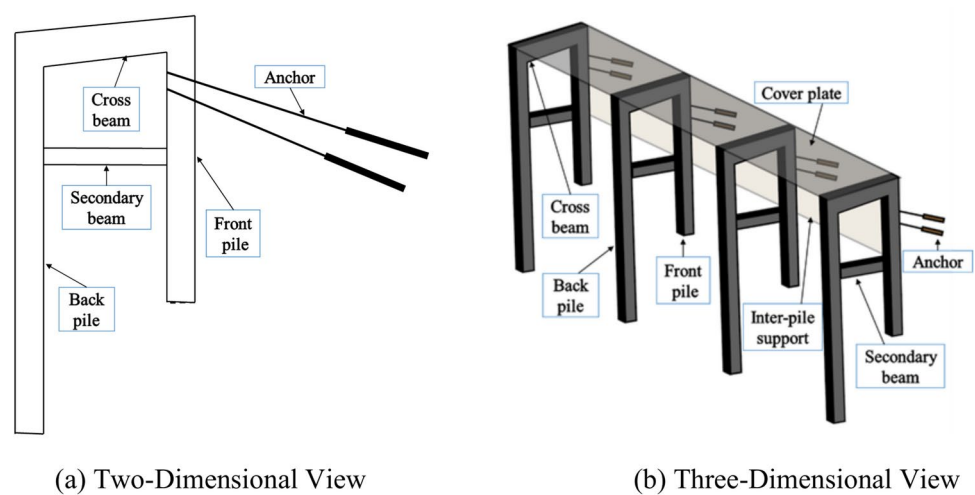
(a) Two-Dimensional View   (b) Three-Dimensional View

Fig. 1. Structural form.

Types	Parameters
Working plat-form size	8.0 m × 10.0 m
Vibration direction	X,Y,Z, six-degree-of- freedom
Loading frequency	0.1–50 Hz
Maximum horizontal displacement	± 800 mm
Maximum vertical displacement	± 400 mm
Maximum horizontal acceleration	1.4 g
Maximum vertical acceleration	1.4 g
Maximum load	160 t
Maximum tilting moment	6000 kN m

Table 1. Main technical parameters of shaking table.

(a) Shaking table (Including control center, actuator system, hydraulic system, and cooling system)

(b) Model box （Including steel plates, angle steel, and channel steel）
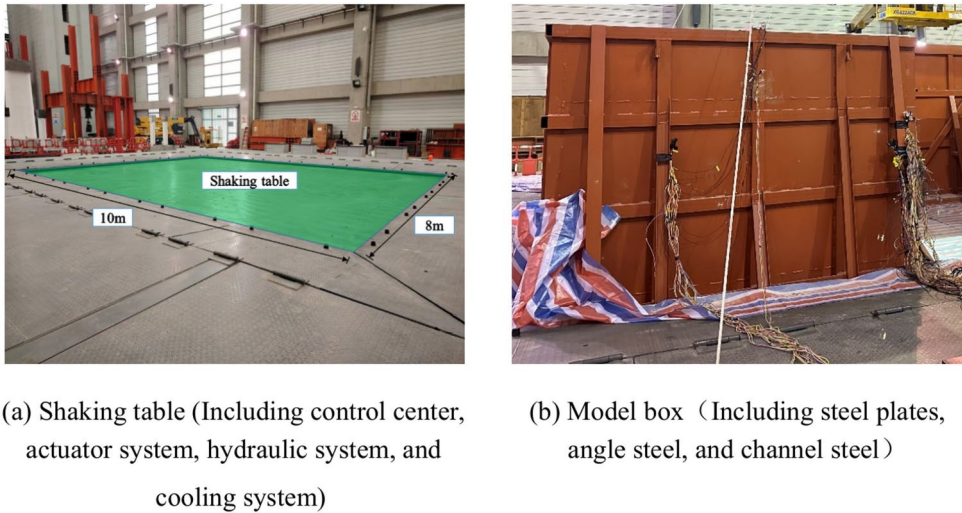
Fig. 2. Shaking table and model box.

Number	Physical quantities	Symbols and relation expression	Similitude parameter	Number	Physical quantities	Symbols and relation expression	Similitude parameter
1	Geometry dimension L	C_l	30	9	Gravity acceleration g	$C_g = 1$	1
2	Density ρ	C_ρ	1	10	Amplitude of input acceleration A	$C_A = 1$	1
3	Duration Td	$C_{Td} = C_l^{0.5}$	5.47	11	Input vibration frequency ω	$C_\omega = C_l^{-0.5}$	0.183
4	Cohesion c	$C_c = C_l$	30	12	Output displacement s	$C_S = C_l$	30
5	Internal friction angle φ	$C_\varphi = 1$	1	13	Output strain ε	$C_\varepsilon = 1$	1
6	Dynamic modulus of elasticity E	$C_E = C_l$	30	14	Output velocity V	$C_V = C_l^{0.5}$	5.47
7	Poisson ratio μ	$C_\mu = 1$	1	15	Output stress σ	$C_\sigma = C_l$	30
8	Shear wave velocity Vs	$C_{Vs} = C_l^{0.5}$	5.47	16	Output acceleration a	$C_a = 1$	1

Table 2. Similarity coefficients of the shaking table test.
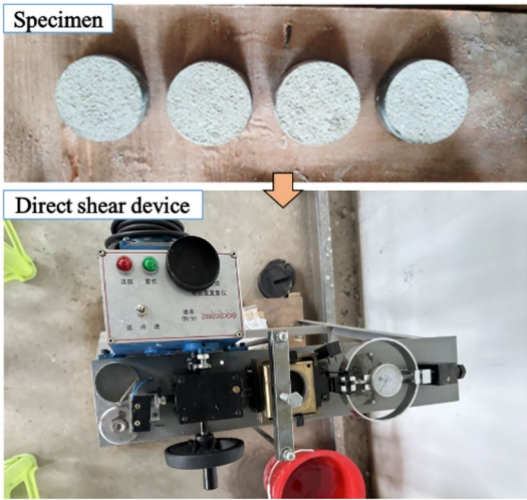

Fig. 3. direct shear test.

	Density (g/cm³)	Elastic modulus(MPa)	Cohesion (kPa)	Internal friction (°)	Poisson ratio	Material ratio
Bedrock	2.2	180	1.9	35	0.18	Barite powder: quartz sand: gypsum: glycerol: water = 30:90:4:1:8
Overburden layer	2.0	12	1.5	30.5	0.22	Loess: quartz sand: water = 4:7:1

Table 3. Material parameters and ratio.

of 10 cm × 7.5 cm and a thickness of 3 mm, while the anchor cables were simulated using thin iron sheets measuring 0.5 mm × 5 mm[16,17].

Model construction and the sensors layout

Firstly, a 10 cm thick foam was attached to the inner wall of the model box to reduce the impact of boundary effects resulting from the rigid model box[25,26]. The contour lines of the model and sensor locations were then drawn on the foam to guide the placement of the filler material. After the raw materials were evenly mixed in the mixer, they were poured into the model box using a forklift and truss car. Compaction was carried out in layers of 15 cm thickness. After each layer was compacted, a ring knife was used to take samples for density testing to control the quality of compaction. When installing the frame piles, start by compacting the soil to 20 cm above the bottom surface of the piles. Next, excavate the trench to place the frame piles and adjust their position. Once the position was confirmed, install the support between the piles and proceed with backfilling. The installation method of anchored solid was the same as that of the frame pile. The anchor cables were connected to the frame piles using connectors. The amount of prestressing was controlled by unscrewing the connector nut. During the layout of the acceleration sensors, fine sand was spread over the sensor surface to ensure that the sensors were exposed to uniform forces. Once the entire slope masonry was completed, the track was installed, and
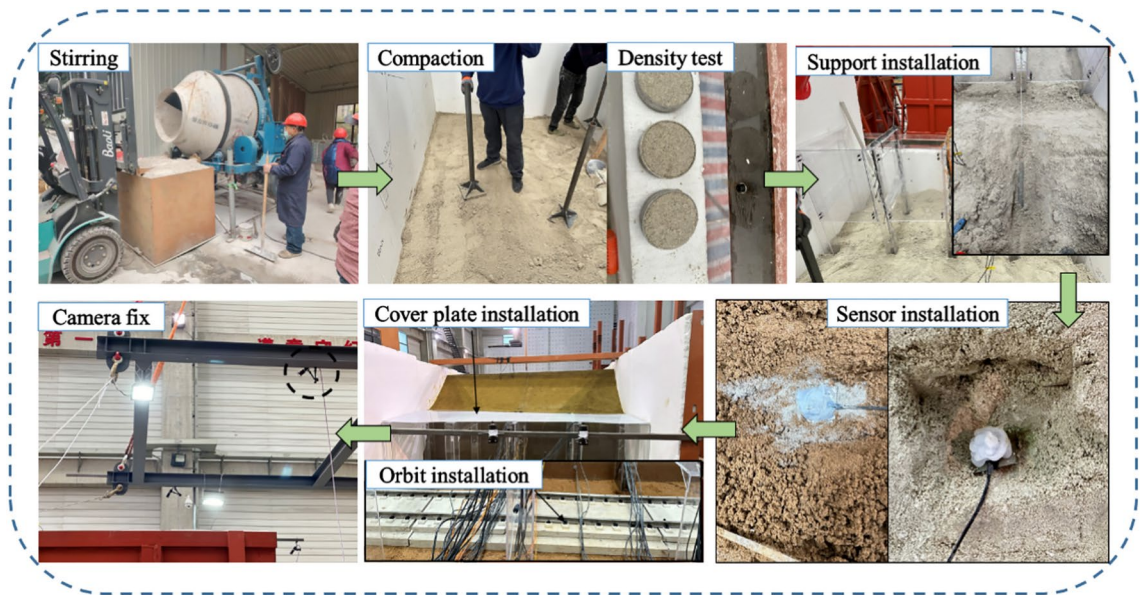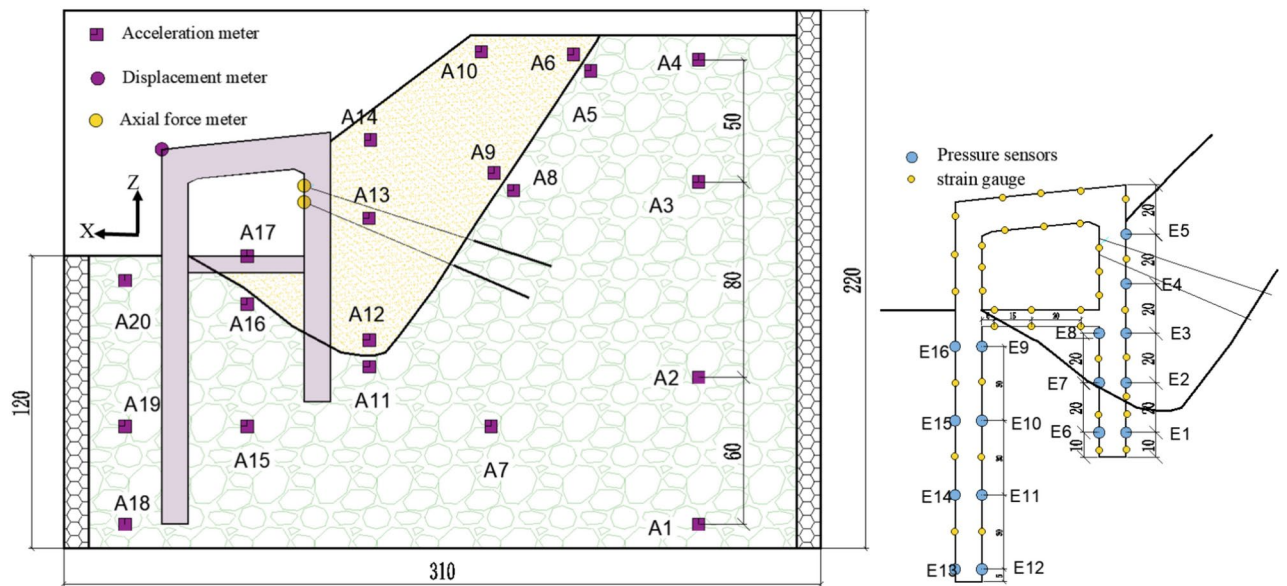
Fig. 4. Masonry process.

Fig. 5. measuring point arrangement.

finally, the cover plate was secured on top of the pile with screws. The masonry process is shown in Fig. 4. To analyze the evolution of the acceleration field in a slope under seismic activity, acceleration meters are uniformly distributed throughout the slope. Additionally, to investigate the differences in vibration between the bedrock and the overburden, acceleration meters are positioned on both sides of the interface. In order to study the forces and deformations of the pile body, 16 soil pressure transducers and 37 strain gauges are uniformly distributed along the pile. Additionally, a displacement meter is positioned at the top of the pile. To investigate the forces exerted on the anchor cable during seismic activity, two axial force gauges are installed at the end of the anchor cable. The arrangement of measuring points is shown in Fig. 5. The slope model is shown in Fig. 6.

Seismic wave input
According to the codes ATC-63 (Applied Technology Council, 2008)[27] and ASCE-7-05 (Minimum Design Loads for Buildings and Other Structures)[28], either man-made seismic waves or actual seismic records can be selected for the time response analysis. The seismic wave input must consist of no fewer than three records. Therefore, three types of seismic wave inputs commonly used in the current study were selected: the Wenchuan Wolong seismic wave, the Kobe seismic wave, and the El Centro seismic wave. To investigate the effect of
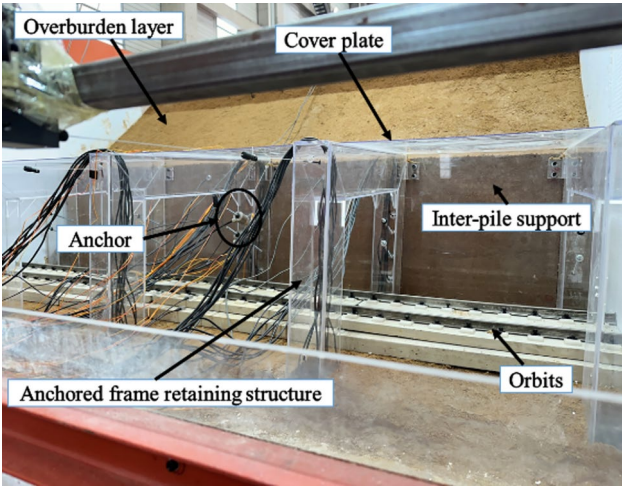
Fig. 6. slope model.

Number	Seismic waveform	Peak acceleration (g)			Number	Seismic waveform	Peak acceleration (g)		
		X	Y	Z			X	Y	Z
1	White noise	0.05	0.05	0.05	17	White noise	0.05	0.05	0.05
2	Kobe	0.1	–	–	18	Kobe	0.8	–	–
3	EL Centro	0.1	0.06	0.06	19	EL Centro	0.8	0.48	0.48
4	Wolong	0.1	0.07	0.09	20	Wolong	0.8	0.56	0.72
5	White noise	0.05	0.05	0.05	21	White noise	0.05	0.05	0.05
6	Kobe	0.2	–	–	22	Kobe	1.0	–	–
7	EL Centro	0.2	0.12	0.12	23	EL Centro	1.0	0.6	0.6
8	Wolong	0.2	0.14	0.18	24	Wolong	1.0	0.7	0.9
9	White noise	0.05	0.05	0.05	25	White noise	0.05	0.05	0.05
10	Kobe	0.4	–	–	26	Kobe	1.2	–	–
11	EL Centro	0.4	0.24	0.24	27	EL Centro	1.2	0.72	0.72
12	Wolong	0.4	0.28	0.36	28	Wolong	1.2	0.84	1.08
13	White noise	0.05	0.05	0.05	29	White noise	0.05	0.05	0.05
14	Kobe	0.6	–	–	30	Kobe	1.4	–	–
15	EL Centro	0.6	0.36	0.36	31	EL Centro	1.4	0.84	0.84
16	Wolong	0.6	0.42	0.54	32	Wolong	1.4	0.98	1.26

Table 4. Loading sequence of the test.

seismic acceleration amplitude on the slope, the amplitudes were set to 0.1, 0.2, 0.4, 0.6, 0.8, 1.0, 1.2, and 1.4 g. Additionally, a 0.05 g white noise was applied before and after each level of seismic wave loading for frequency sweeping. The specific order of imposition is shown in Table 4. In consideration of space limitations, this paper chooses to analyze the Wolong wave loading condition in detail. The acceleration time-history curve and Fourier spectrum of the Wolong wave in three directions are shown in Fig. 7.

Results
Experimental phenomena
In this section, the Particle Image Velocimetry (PIV) technique was used to analyze the deformation of slopes during earthquakes. PIV technology can effectively observe the movement trends of particles[29–32]. This section analyzes the changes in the displacement field of the slope under 0.2, 0.4, 0.6, and 0.8 g earthquakes using PIV based on the initial state image. The variation of the slope displacement field is shown in Fig. 8. When the input peak seismic acceleration was 0.2 g, the displacement of the trailing edge of the slope was the most pronounced, while the deformation of the soil behind and between the piles was relatively minor. When the seismic intensity reached 0.4 g, the displacement of the trailing edge of the slope increased significantly, and the deformation of the soil between the piles on the right side increased in comparison to the soil behind the piles. At this point, cracking occurs at the trailing edge of the slope along the soil-rock interface, as illustrated in Fig. 9a. When the seismic intensity reached 0.6 g, the soil deformation between the piles on the left side also increased. At this time, the cracks at the trailing edge of the slope widened, and localized cracks appeared on the slope, as illustrated in
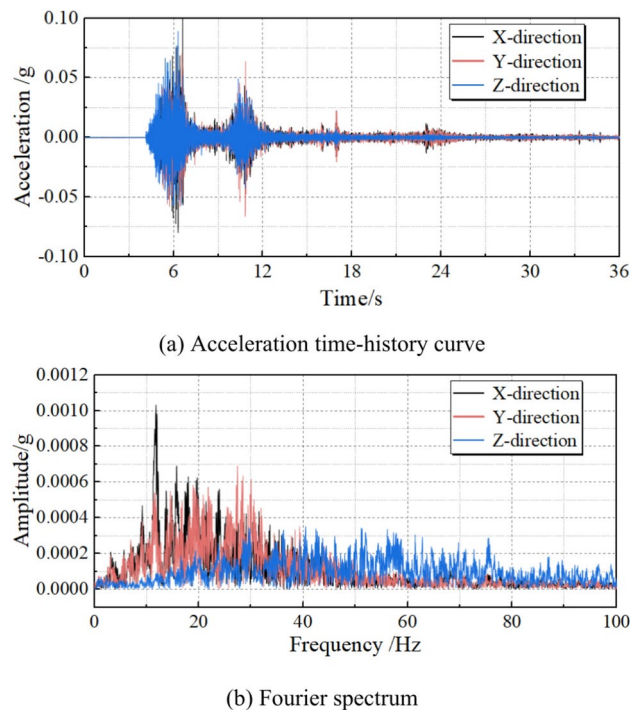
(a) Acceleration time-history curve

(b) Fourier spectrum

Fig. 7. Wolong seismic wave time-history curve and Fourier spectrum.

Fig. 9b. When the seismic intensity reached 0.8 g, all the inter-pile soils were significantly larger than the post-pile soils. It can be seen that the overall soil displacement at the rear of the support structure was less than that at the rear edge of the slope throughout the loading process. The soil at the trailing edge of the slope continuously squeezed forward on the leading edge, causing deformation of the pile-slab structure, from which it can be inferred that the slip surface of this type of slope may developed from the trailing edge of the slope to the leading edge. As the seismic action increased, the piles limit the slope displacement more than the inter-pile supports, resulting in greater deformation of the inter-pile supports than the piles. The pile bent and squeezed the soil in front of the pile, resulting in cracking and crushing of the soil. Longitudinal cracking was observed at the slope face, which may be due to greater deformation of the inter-pile support than the pile, resulting in simultaneous shear misalignment in the longitudinal direction while the overburden layer slid.

Laws of acceleration field evolution within the slope

To analyze the influence of seismic intensity on the amplification of peak acceleration of bedrock and overburden layer slope under three-directional seismicity, the horizontal and vertical acceleration amplification coefficients of the internal measurement points of the slopes under the peak values of the input seismic wave of 0.2 g, 0.4 g, 0.6 g, and 0.8 g conditions were selected for the study in this part. Firstly, the acceleration data were band-pass 0–50 Hz filtered and baseline correction processed to obtain the peak value of the acceleration time-history curve, subsequently, the ratio of the peak acceleration of the measurement point to the measurement point A1 was used as the amplification coefficient of the point, and the cloud diagram of the amplification coefficient of the model acceleration was obtained through the linear interpolation method, as shown in Figs. 10 and 11.

When the peak acceleration of the input seismic wave was 0.2 g, the horizontal acceleration amplification coefficient inside the slope was relatively uniformly distributed and increased with the increase of elevation. The horizontal acceleration amplification coefficient of the slope decreased with increasing seismicity and there was always a concentration zone of acceleration at the slope shoulder. The amplification coefficients for the concentration zone of horizontally oriented acceleration during seismic actions of 0.2 g, 0.4 g, 0.6 g, and 0.8 g range from 4.006 to 4.77, 3.966 to 4.73, 2.904 to 3.43, and 2.078 to 2.44, respectively. When the peak value of the input seismic wave acceleration was 0.8 g, the acceleration concentration zone appeared in front of the pile. The formation of the acceleration concentration zone in front of the pile may be due to the sliding of the overburden layer squeezing the frame pile, and the bending of the frame pile squeezing the soil in front of the pile, which made the soil broken and then affected the contact between the acceleration sensor and the soil, and results in severe vibration during seismic action. The amplification coefficient of acceleration in the horizontal direction was significantly larger than that in the vertical direction. As the seismic action increased, the concentration of the vertical acceleration amplification coefficient shifted from the back of the pile to the top of the slope. The acceleration amplification coefficient of the overburden layer was always greater than that of the bedrock during the loading process, which resulted in the difference in vibration amplitude between the two, making the bedrock and the overburden layer vibration inconsistent. From the figure, it can be seen that the variability of
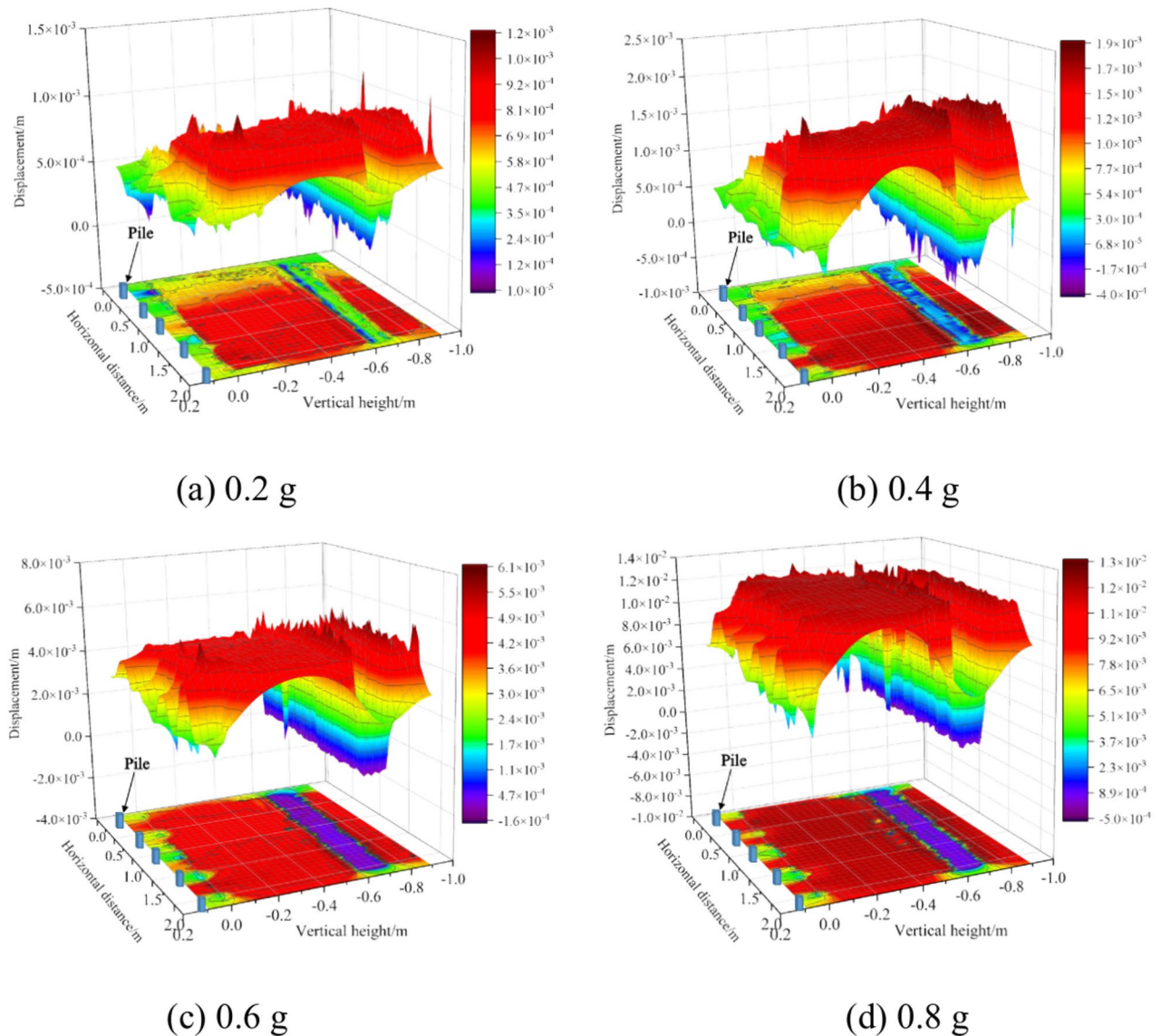
(a) 0.2 g

(b) 0.4 g

(c) 0.6 g

(d) 0.8 g

Fig. 8. Characterization of slope displacement field evolution.

bedrock and overburden vibration near the anchor cable was small, and the anchor cable was able to improve the consistency of bedrock and overburden vibration.

Analysis of bedrock-overburden layer vibration differences on both sides of the interface

The variability of bedrock and overburden vibration could be one of the reasons for the occurrence of landslides, therefore, this part analyzed the variability of bedrock and overburden vibration at the interface of different locations. A5 and A6 were located at the top of the slope and A9, A8, A12, and A11 were located near the anchor cables. The peak acceleration amplification coefficient was the ratio of the peak acceleration of the interfacial overburden layer to the peak acceleration of the bedrock. As shown in Figs. 12 and 13. The difference in vibration between the two sides of the interface in the vicinity of the anchor cable decreased with increasing seismicity under horizontally oriented seismic action. The difference in vibration between the two sides of the interface near the anchor cable under vertical seismic activity tended to decrease with increasing seismic intensity. This may be because as the seismic action increased, the coordination between the pile and the anchor cable increased and the slip resistance provided by the increase in the axial force of the anchor cable increased, thus leading to a decrease in the variability of the vibration between the bedrock and the overburden layer. Near the top of the slope away from the anchor cables, the variability of vibration on both sides of the interface showed a tendency to increase and then decrease with the increase of the seismic intensity under the horizontally oriented earthquakes, but the values remained at a high level. Under vertical seismicity, the variability of vibration on both sides of the interface at the top of the slope increased gradually with the increase of seismic intensity. The experimental phenomena indicated severe damage at the top of the slope, which may be due to the gradual increase in the variability of vibration of the bedrock and the overburden layer at the top of the slope.
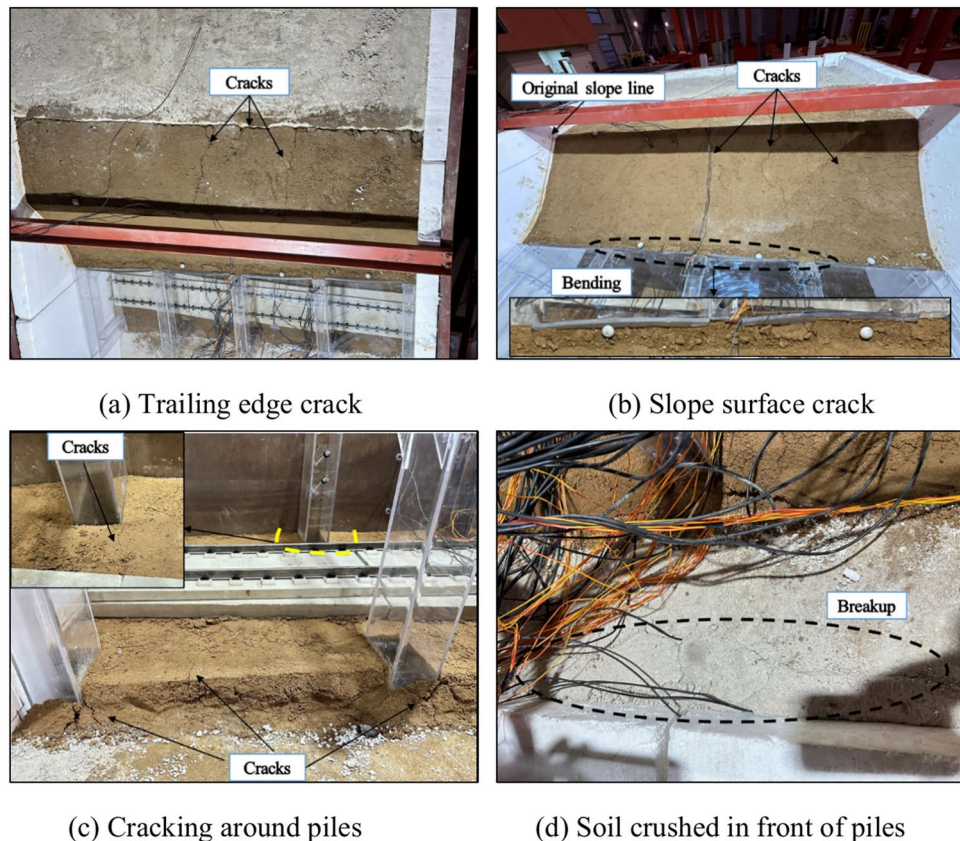
(a) Trailing edge crack

(b) Slope surface crack

(c) Cracking around piles

(d) Soil crushed in front of piles

Fig. 9. Destruction of slope.

To further analyze the variability of vibration between bedrock and overburden layer, the acceleration data of A5, A6, A9, and A8 under 0.6 g seismic action were Fourier transformed. As shown in Figs. 14 and 15. A5 and A8 were located within the bedrock, and A6 and A9 were located within the overburden layer. At the location of the top of the slope, the amplitude of the high-frequency part of the Fourier spectrum of the overburden layer was greater than that of the bedrock in all cases. The main frequency of the Fourier spectrum for any point in the Y-direction was 11.7687 Hz, while there was a small difference in the main frequency of the Fourier spectrum in the Z-direction between the bedrock and the overburden layer. It can be seen that the difference in frequency and amplitude of vibration between the overburden layer and bedrock was one of the important factors in slope failure.

Dynamic soil pressure of frame pile

To analyze the dynamic soil pressure distribution around the frame piles under seismic action, 16 soil pressure sensors were uniformly placed in front of and behind the piles. The distribution curves of the dynamic soil pressure along the elevation of the front and back pile for different intensity earthquakes are shown in Figs. 16 and 17. The bottom of the model box was used as the elevation zero point. The dynamic soil pressure values were highest at the bottom of the pile in front of the front piles, followed by the top, and gradually increased with increasing seismic action. The slope damage is significant at 0.6 g, with the peak dynamic soil pressure at the top of the front pile measuring 9.5 kPa and the peak dynamic soil pressure at the bottom measuring 24.3 kPa. The peak dynamic soil pressure behind the front pile occurred near the slip surface and increased gradually with increasing seismic action. The peak dynamic soil pressures for both the front and back of the back pile occurred at the top and were essentially zero at the remaining locations. The overall deformation of the back pile was minimal. The soil in front of the pile sustained significant damage at 0.8 g. At this moment, the peak dynamic soil pressure in front of the pile, at the top of the anchored section, was 2.8 kPa, while the peak dynamic soil pressure behind the pile reached 9.9 kPa. This may be due to the sliding of the overburden layer behind the piles along the sliding surface squeezing the frame piles, the overall bending of the front piles, and the squeezing of the bedrock at the bottom of the piles toward the overburden layer, resulting in the highest peak dynamic soil pressure at the bottom of the front piles in front of the piles. The rear part of the pile will squeeze the soil behind the pile when the front pile rotates. The bedrock is stiffer than the overburden layer, causing the bottom of the pile to move forward, reaching its maximum value at the slip surface. The anchor cable had a limiting effect on the displacement of the pile. When the peak acceleration reached 0.6 g, the deformation coordination between the pile and the anchor cable increased significantly leading to an increase in the value of dynamic soil pressure
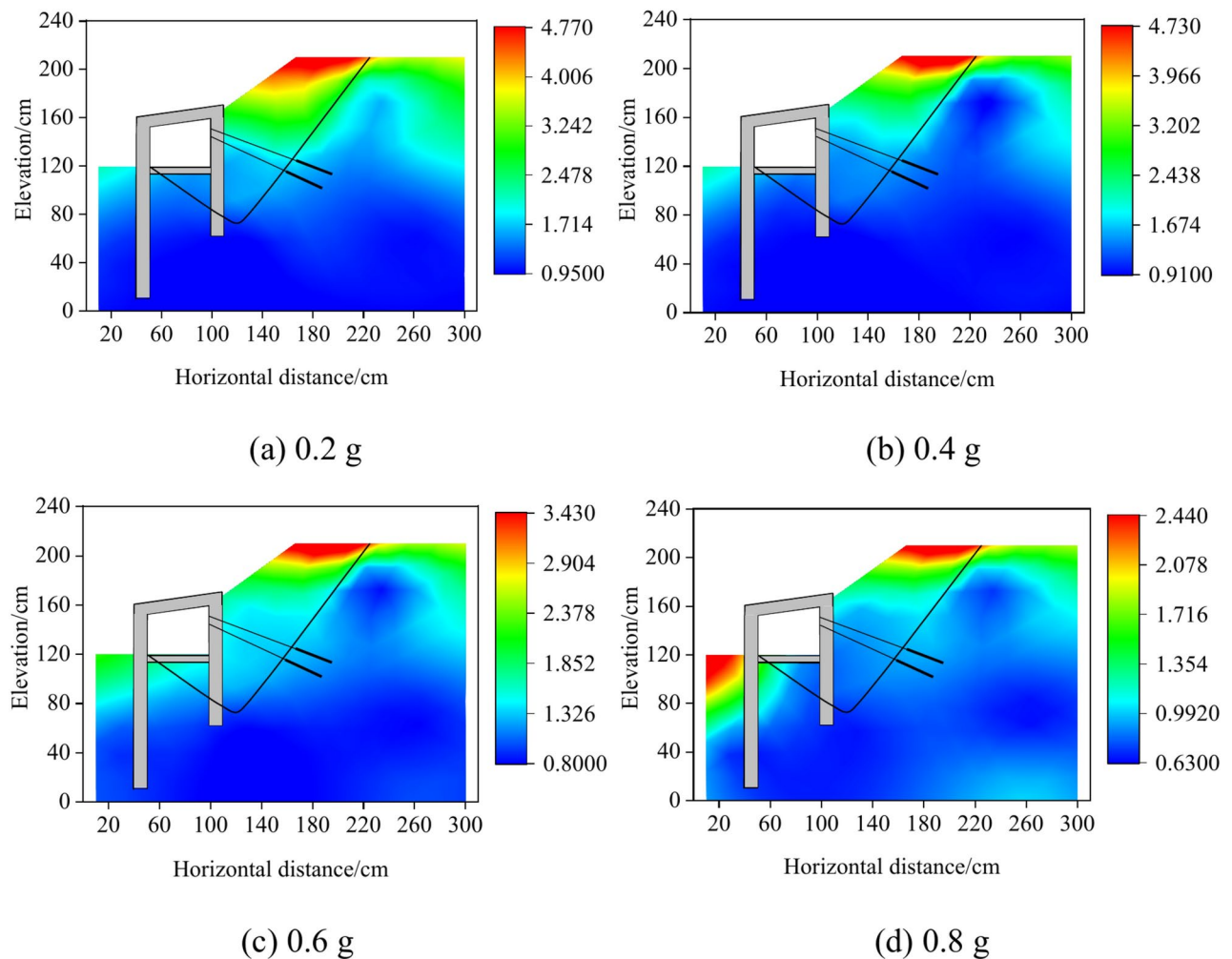
(a) 0.2 g

(b) 0.4 g

(c) 0.6 g

(d) 0.8 g

Fig. 10. Distribution of X-direction Peak acceleration amplification factor in different earthquake intensity.

at the top of the front pile. The rear pile was bent, and the bottom of the pile did not move, extruding the top of the bedrock in front of the pile resulting in the highest peak dynamic soil pressure at the top.

Anchor cable axial force and displacement of pile top

To analyze the variation of the axial force of the anchor cable under seismic action, the peak values of the anchor cable of the frame pile in the middle of the model under the seismic action of 0.1, 0.2, 0.4, 0.6, 0.8, and 1.0 g were selected for analysis. As shown in Fig. 18. The peak displacement increment curve at the top of back pile under different earthquake intensities is shown in Fig. 19. When the seismic acceleration was less than 0.4 g, the axial force of the two rows of anchor cables was the same, and the change was small with the increase of seismic action. When the peak acceleration reached 0.4 g, the displacement at the top of the pile increased, resulting in bending deformation of the pile body, which caused a slight increase in the tension of the upper row of anchor cables. When the peak acceleration reached 0.6 g, the axial force of the upper row of anchor cable suddenly increased, the displacement at the top of the pile increased further, indicating that the significant increase in the displacement of the overburden layer led to an increase in the deformation of the pile, and the pile-anchor synergistic effect was obvious, which led to an increase in the axial force of the anchor cable. As the pile undergoes bending deformation, the upper displacement was greater than the lower, so the upper anchor cable deformation value was greater than the lower, resulting in a greater axial force value than the lower. With a further increase in seismic action, the values of axial force in both rows of anchor cables increased substantially. When the peak seismic acceleration reached 1.0 g, the peak axial force of both rows of anchor cables decreased, which may be due to the sliding of the anchoring section of the anchor cables, resulting in a reduction of the anchoring force, which led to a reduction of the anchor deformation retraction tension.

Track board vibration response

To analyze the safety of traveling under seismic effects, this test pasted two accelerometers at the same horizontal position on the top of the track plate and the base, to analyze the difference between the two vibrations. In this section, the peak accelerations and differentials in the direction of the main vibration of the track slab and base
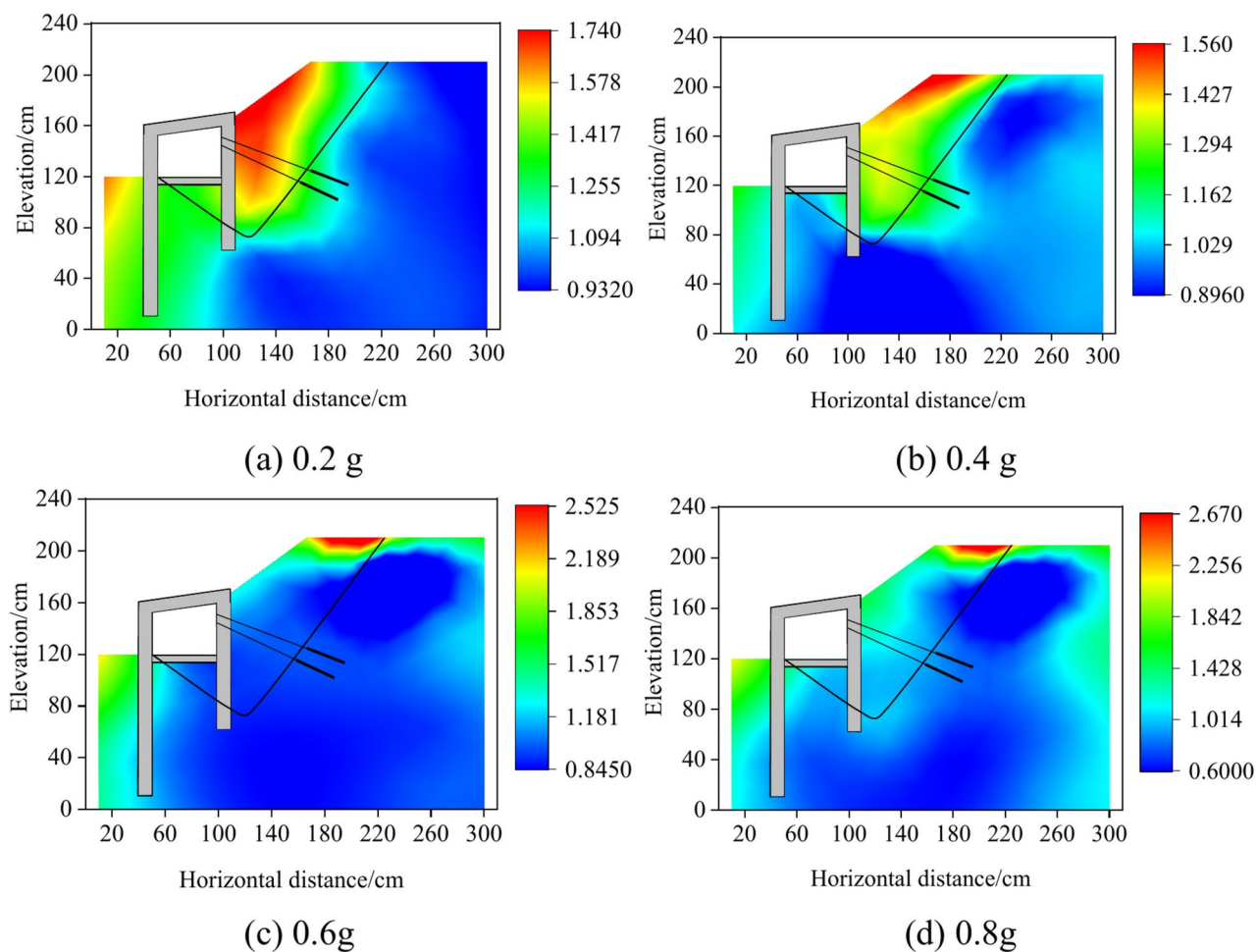
Fig. 11. Distribution of Z-direction Peak acceleration amplification factor in different earthquake intensity.
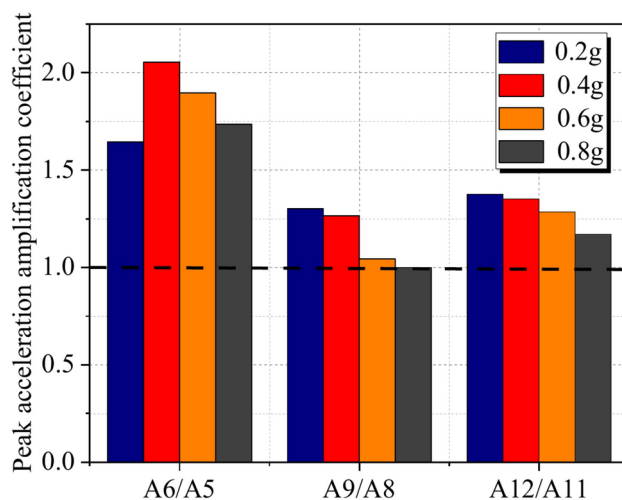

Fig. 12. Comparison of horizontal acceleration at the overburden layer-bedrock interface.

under 0.1, 0.2, 0.4, 0.6, 0.8, and 1.0 g earthquakes were selected for analysis. As shown in Fig. 20. When the seismic acceleration did not exceed 0.4 g, the peak acceleration of both the track plate and the base were the same, and the vibration consistency was good. When the seismic acceleration exceeded 0.4 g, the vibration variability between the two increased. When the seismic acceleration reached 1.0 g, the difference between the
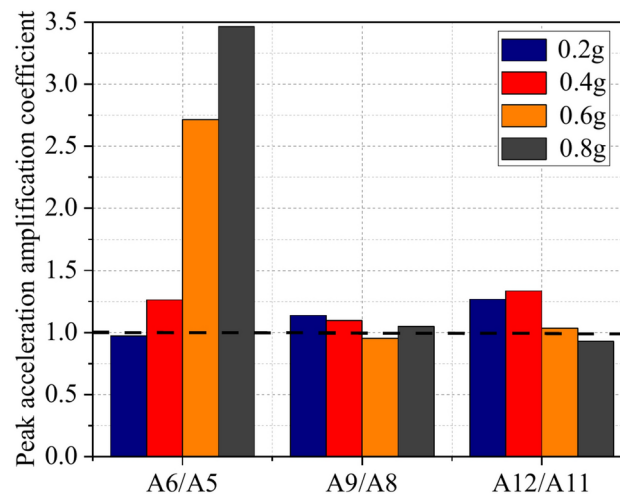
Fig. 13. Comparison of vertical acceleration at the overburden layer-bedrock interface.
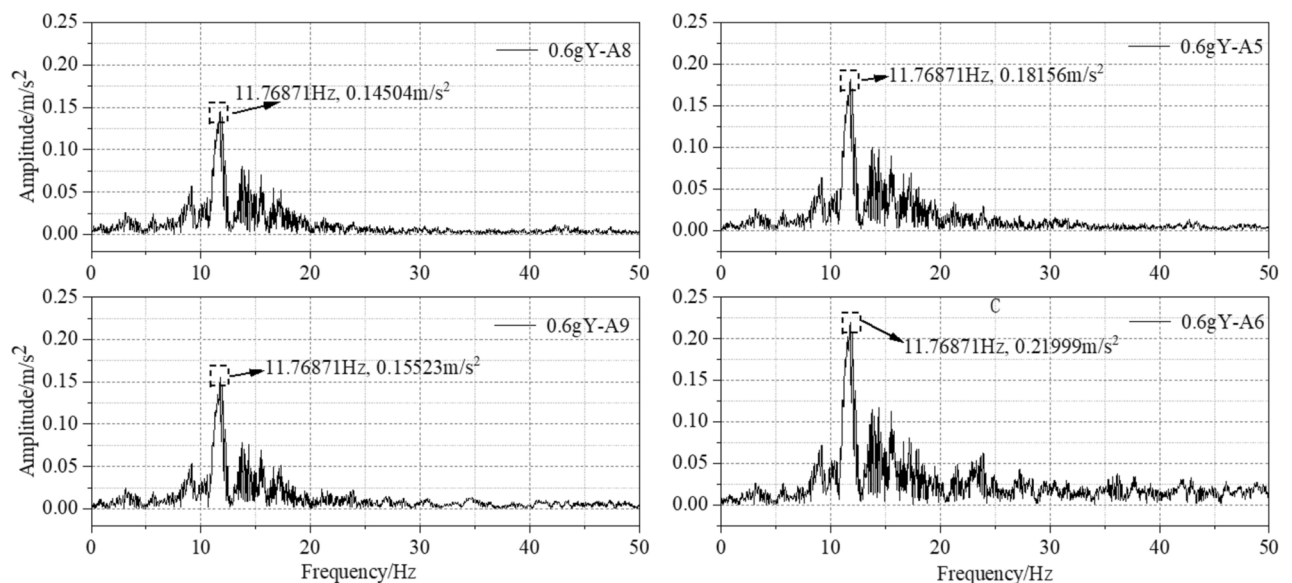
Fig. 14. Fourier spectrum of acceleration in X-direction.

two peak accelerations reached 0.261 g. The damage in the traveling area at the end of the test loading is shown in Fig. 21. During seismic action, the inconsistency between the vibration of the track plate and the base caused the track plate and the base to deflect. The bolts around the orbit have localized detachment, and the track joints were shifted, which seriously affected the smoothness of travel. Therefore, the seismic effect should be predicted in warning, so that the train stopped in advance braking to ensure the safety of personnel.

Conclusion

In this study, three-way seismic loading was carried out on bedrock and overburden layer slope reinforced by anchored frame piles, and the following conclusions were drawn from the acceleration amplification coefficient, the variability between bedrock and overburden layer, the pile forces and the damage phenomena.

(1) A zone of acceleration concentration exists at the shoulder of a slope under seismic action. Anchor cables have a significant effect on reducing the variability of bedrock and overburden layer vibrations. The vibration variability of bedrock and overburden at the top of the slope away from the anchor cable is consistently high. Emphasis should be placed on reinforcing areas of concentrated acceleration to ensure that the overburden vibrates in unison with the bedrock. The slip surface of the model under seismic action develops through from the trailing edge to the leading edge. The track plate is deflected by the inconsistency of the vibration of the track plate and the base during seismic action.
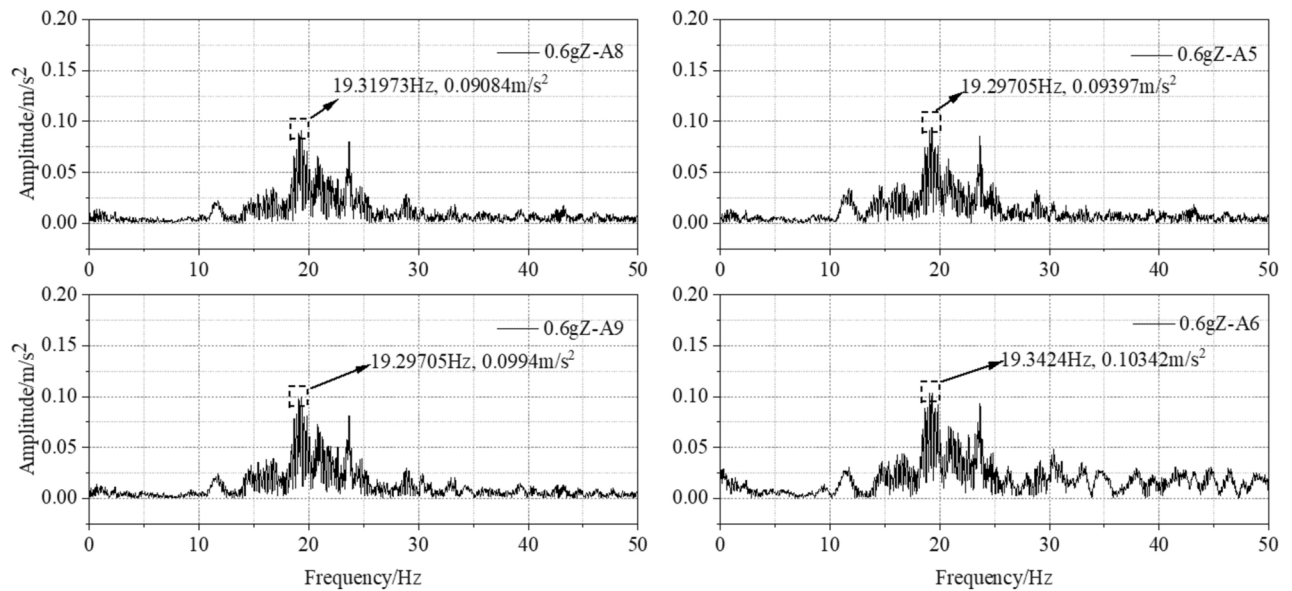
Fig. 15. Fourier spectrum of acceleration in Z-direction.

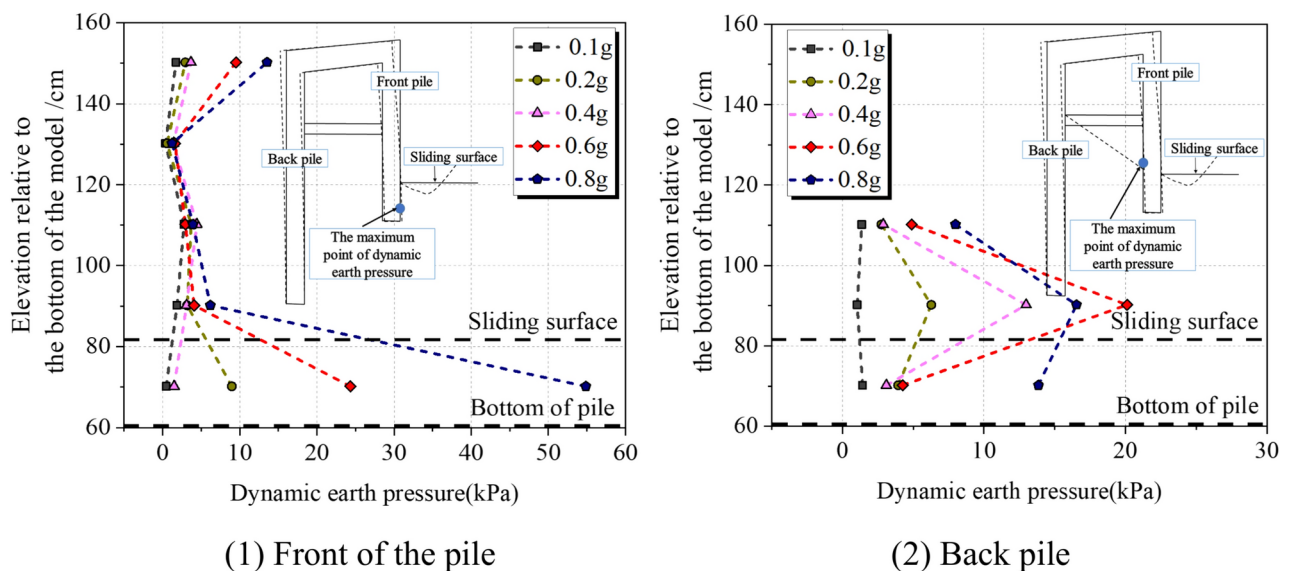(1) Front of the pile   (2) Back pile

Fig. 16. Front pile dynamic soil pressure change law.

(2) Under seismic action, the front pile of the anchored frame pile bends as a whole while the bottom of the pile squeezes the bedrock forward, and the back pile undergoes overall bending and squeezes the soil in front of the pile. The anchored frame piles limit the overburden layer displacement more strongly than the inter-pile supports, which undergo significant bending damage, The design aims to maintain consistent stiffness in both the anchored frame piles and the inter-pile supports.

(3) Under seismic action, the peak dynamic earth pressure in front of the front pile occurs near the bottom of the pile, and the dynamic earth pressure behind the pile occurs near the slip surface. The peak dynamic earth pressure of the back pile occurs at the top of the bedrock. Elevating the prestressing and anchoring force of the anchor cables will help to increase the synergy between the anchor cables and the piles, which in turn will limit the displacement of the piles, reduce the damage of the soil in front of the piles, and improve the overall stability of the slope-structure.
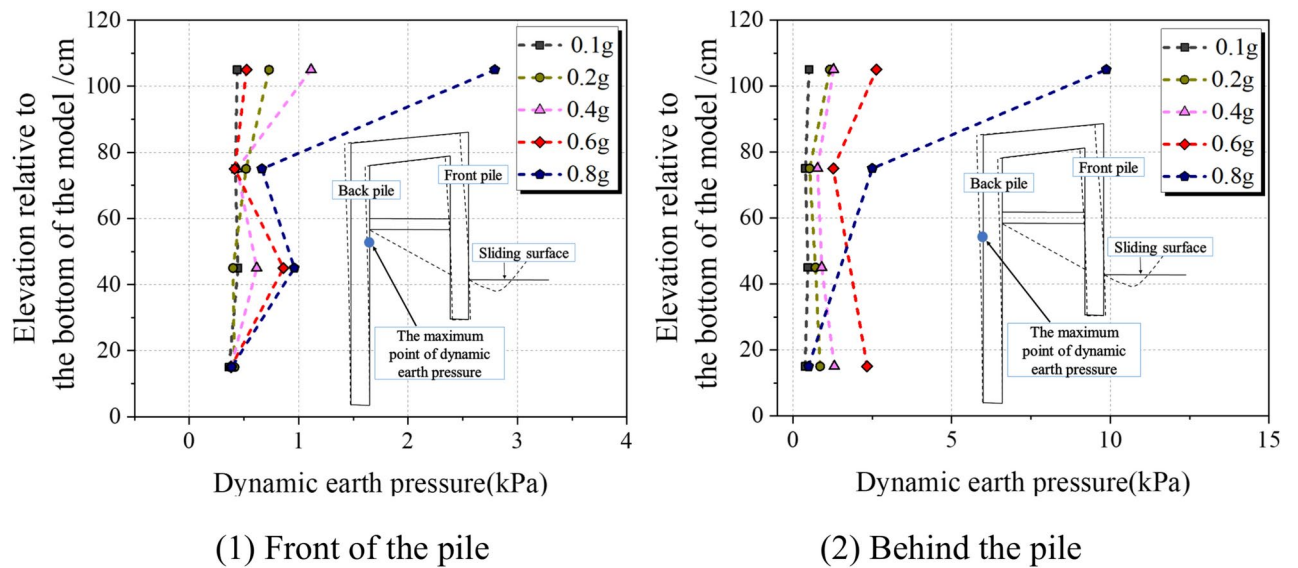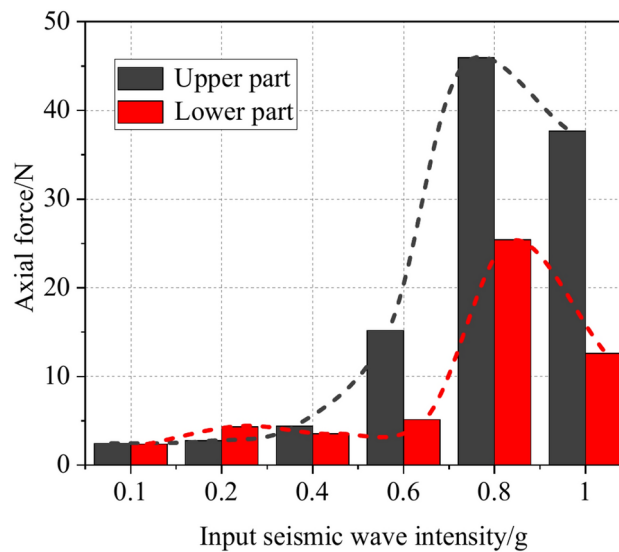
Fig. 17. Back pile dynamic soil pressure change law.

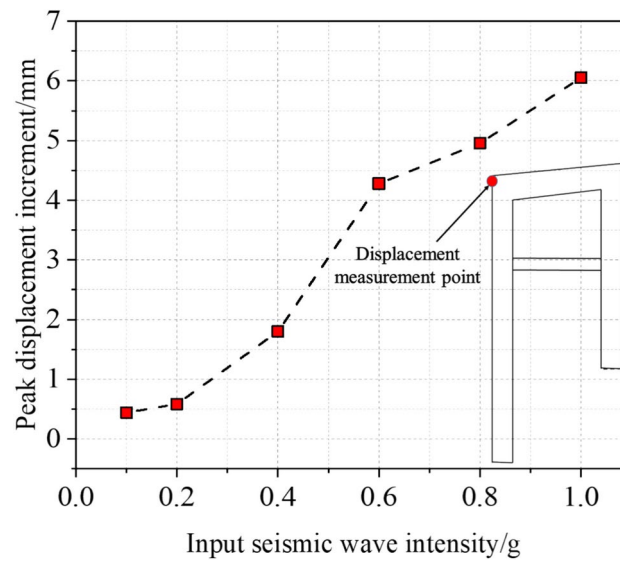**Fig. 18**. Change in peak anchor cable axial force.

Fig. 19. The peak displacement increment curve at the top of back pile under different intensity earthquakes.
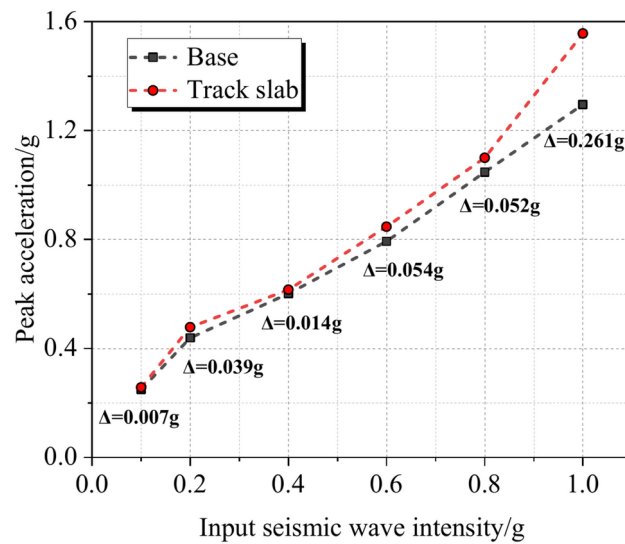

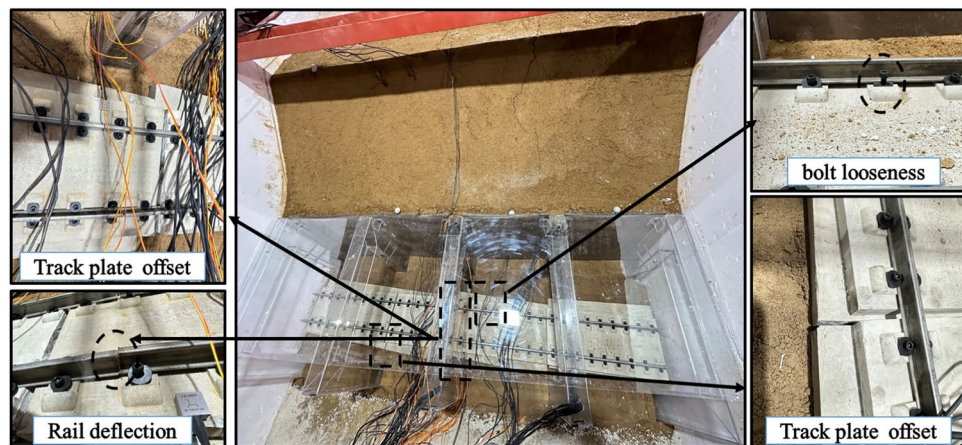**Fig. 20**. Difference in vibration of track plate-base.

Fig. 21. Track plate damage.

Data availability

The data used to support the findings of this study are available from the corresponding author upon request.

References

1. Huang, Y., Xu, X. & Mao, W. W. Numerical performance assessment of slope reinforcement using a pile-anchor structure under seismic loading. *Soil Dyn. Earthq. Eng.* **129**, 10596 (2020).
2. Zhao, T. et al. Analysis of slope stability with dynamic overloading from earthquake. *J. Earth Sci* **23**, 285–296 (2012).
3. Li, H. H. et al. Dynamic response of a dip slope with multi-slip planes revealed by shaking table tests. *Landslides* **15**, 1731–1743 (2018).
4. Cao, L. et al. Dynamic response and dynamic failure mode of the slope subjected to earthquake and rainfall. *Landslides* **16**, 1467–1482 (2019).
5. Pai, L. F. & Wu, H. G. Shaking table test of comparison and optimization of seismic performance of slope reinforcement with multi-anchor piles. *Soil Dyn. Earthq. Eng.* **145**, 106737 (2021).
6. Wu, Z. J. et al. Dynamic response characteristics and failure mode of slopes on the loess tableland using a shaking-table model test. *Landslides* **17**, 1561–1575 (2020).
7. Yang, Z. et al. Experimental study on dynamic characteristics and dynamic responses of accumulation slopes under frequent microseisms. *Arab. J. Geosci.* **13**, 770 (2020).
8. Lv, Q. C., Liu, Y. R. & Yang, Q. Stability analysis of earthquake-induced rock slope based on back analysis of shear strength parameters of rock mass. *Eng. Geol.* **228**, 39–49 (2017).
9. Ye, W., Zhou, Y. & Ye, S. Dynamic stability analysis of frame anchor-supported slope. *Arab. J. Geosci.* **14**, 1489 (2021).
10. Xue, L. et al. A multi-objective optimization evaluation model for seismic performance of slopes reinforced by pile-anchor system. *Sci. Rep.* **14**, 5044 (2024).
11. Hu, H. Q. et al. Shaking table tests on slope reinforced by anchored piles under random earthquake ground motions. *Acta Geotech.* **17**(9), 4113–4130 (2022).
12. Dong, J. H., Wu, X. L. & Lian, B. Study on dynamic calculation method for landslide prevention structure of anti-slide pile with pre-stressed anchor cable. *China Civil Eng. J.* **55**(11), 72–82 (2022).
13. Xu, X. & Huang, Y. Parametric study of structural parameters affecting seismic stability in slopes reinforced by pile-anchor structures. *Soil Dyn. Earthq. Eng.* **147**, 106789 (2021).
14. Hu, H. Q. et al. Investigation of seismic behavior of slope reinforced by anchored pile structures using shaking table tests. *Soil Dyn. Earthq. Eng.* **201**(Nov.), 150 (2021).
15. Dong, X. G. et al. Stability analysis of the pile-prestressed anchor composite structure based on failure mode. *Eng. Fail. Anal.* **137**, 106223 (2022).
16. Qu, H. L., Luo, H., Hu, H. G., Jia, H. Y. & Zhang, D. Y. Dynamic response of anchored sheet pile wall under ground motion: Analytical model with experimental validation. *Soil Dyn. Earthq. Eng.* **115**, 896–906 (2018).
17. Chen, G. P. et al. Shaking table test and numerical analysis of dynamic response and damage mechanism of a deposit slope with a weak interlayer reinforced by a pile–anchor structure. *Structures* **59**, 105728 (2024).
18. Chen, G. P. et al. Shaking table test on dynamic response of a deposit slope with a weak interlayer reinforced by the pile-anchor structure. *Soil Dyn. Earthq. Eng.* **170**, 107912 (2023).
19. Lian, J. et al. Dynamic responses and evolution characteristics of bedrock and overburden layer slope with space anchor cable anti-slide piles based on large-scale shaking table test. *Soil Dyn. Earthq. Eng.* **175**, 108245 (2023).
20. Yang, C. W. et al. Research on the difference of dynamic response between bedding and toppling rock slopes based on shaking table test. *Chinese J. Rock Mech. Eng.* **41**(02), 271–281 (2022).
21. Li, L. Q. et al. Shaking table test to assess seismic response differences between steep bedding and toppling rock slopes. *Bull. Eng. Geol. Environ.* **78**, 519–531 (2017).
22. Wu, Z. et al. Dynamic-response characteristics and deformation evolution of loess slopes under seismic loads. *Eng. Geol.* **267**, 105507 (2020).
23. Liu, S. L. et al. Shaking table model test and numerical analysis of the bedding rock slopesunder frequent micro-seismic actions. *Chinese J. Rock Mech. Eng.* **37**(10), 2264–2276 (2018).
24. Buckingham, M. An exact solution to the ideal, 3-D wedge as a proposed benchmark. *J. Acoust. Soc. Am.* https://doi.org/10.1121/1.2023772 (1986).

25. Su, L. J., Li, C. & Zhang, C. L. Large-scale shaking table tests on the seismic responses of soil slopes with various natural densities. *Soil Dyn. Earthq. Eng.* **140**, 106409 (2021).
26. Zhang, C. L. et al. Large-scale shaking table model test on seismic performance of bridge-pile-foundation slope with anti-sliding piles: a case study. *Bull. Eng. Geol. Environ.* **79**, 1429–1447 (2020).
27. Applied Technology Council[M]. Redwood, CA: ATC-63, 3–30 (2008).
28. The Federal Emergency Management Agency[M]. Washington, D.C: American Society of Civil Engineers (ASCE), FEMA-356, 15–64 (2000).
29. Reza Abdi, M. et al. Assessment of pegged geogrid (PG) pullout performance in coarse-grained soils using PIV analysis. *Geotext. Geomembr.* **52**, 27–45 (2024).
30. Baba, H. O. & Peth, S. Large scale soil box test to investigate soil deformation and creep movement on slopes by Particle Image Velocimetry (PIV). *Soil Tillage Res.* **125**, 38–43 (2012).
31. Xq, F. et al. Shaking table test on underwater slope failure induced by liquefaction. *Soils Found* **63**, 101357 (2023).
32. Luo, Z. G., Ding, X. M. & Ou, Q. Bearing capacity and deformation behavior of rigid strip footings on coral sand slopes. *Ocean Eng.* **267**, 113317 (2023).

Acknowledgements

Author contributions

L.W.: Investigation, Results analysis, Writing. G.P.C.: making scientific figures, Results analysis, formal analysis. Q.H.P.: review and editing, and project administration. M.M.D.: Results analysis, formal analysis. C.W.Y: review and editing, and project administration. J.L.: Results analysis, formal analysis. All authors reviewed the manuscript.

Declarations

Competing interests

The authors declare no competing interests.

Additional information

Correspondence and requests for materials should be addressed to J.L.

Reprints and permissions information is available at www.nature.com/reprints.

Publisher's note Springer Nature remains neutral with regard to jurisdictional claims in published maps and institutional affiliations.